European Conference on Computational Fluid Dynamics
ECCOMAS CFD 2006
P. Wesseling, E. Oñate and J. Périaux (Eds)

NOISE SOURCES IN SINGLE AND COAXIAL JETS

Elmar Gröschel *, Wolfgang Schröder and Matthias Meinke

Institute of Aerodynamics, RWTH Aachen University
Wüllnerstr. zw. 5 u. 7 , 52062 Aachen, Germany
*Re-mail: e.groeschel@aia.rwth-aachen.de

Key words: Computational Aeroacoustics, Acoustic Perturbation Equations, Jet noise, Single Jet, Coaxial Jet

Abstract. *The acoustic simulations of a cold single stream jet at Mach number 0.9 and Reynolds number 3,600 and two heated coaxial jets at Mach number 0.9 and Reynolds numbers 3,600 and 400,000 are performed. The computation of the acoustic field is performed by a two-step approach using a large-eddy simulation (LES) for the flow field and approximate solutions of the acoustic perturbation equations (APE) for the acoustic field. The purpose of the paper is to identify the effect by heating and the impact of the Reynolds number on the flow field and the acoustic field. The computation of the single jet is validated against the numerical and experimental findings reported in the literature [4, 5, 20]. It is shown that the Lamb vector of the APE-4 formulation is the dominant source term. Compared to the cold single jet, the heated coaxial jets show an enhanced exchange and mixing of fluid due to the temperature and density gradients between the primary and secondary stream. Additional source terms such as temperature and entropy fluctuations and heat release are excited and contribute significantly to the noise radiation in the direction normal to the jet axis producing a dipole-like far field signature. The acoustic field generated by these source terms is Reynolds number dependent, while the acoustic field generated by the Lamb vector is only weakly affected.*

1 Introduction

In general, today's aircraft engines possess dual stream jets in which a hot high-speed primary flow is surrounded by a cold secondary flow. Compared with single jets, coaxial jets with round nozzles can develop flow structures of very different topology, depending on environmental and initial conditions and, of course, on the temperature gradient between the inner or core stream and the bypass stream. Not much work has been done on such jet configurations and as such there are still many open questions [2]. For instance, how is the mixing process influenced by the development of the inner and outer shear layers? What is the impact of the temperature distribution on the mixing and on the noise generation mechanisms?

The present study applies a hybrid method to predict the noise from turbulent jets. It is based on a two-step approach using a large-eddy simulation (LES) for the flow field and approximate solutions of the acoustic perturbation equations (APE) [3] for the acoustic field. The LES comprises the neighborhood of the potential cores and the spreading shear layers. In a subsequent step, the sound field is calculated for the near field, which covers a much larger area than the LES source domain.

The influence of the temperature gradient on the acoustic field at various Reynolds numbers will be investigated. For this purpose, three jets, a cold single and two heated coaxial jets, are simulated. The single jet at Reynolds number 3,600 and Mach number 0.9 matches exactly the flow conditions of the numerical simulation by Freund [4] and the experimental study by Stromberg et al. [5]. It is used to validate the proposed hybrid method and serves as a reference solution for the analysis of the heated coaxial jets.

The first coaxial jet possesses a Reynolds number 3,600 and the second coaxial jet a Reynolds number 400,000 based on the diameter and the velocity of the secondary stream. In a recent study [6] on aeroacoustics of hot jets at various Reynolds numbers it was shown that the spectral shape at high jet temperatures is due to Reynolds number effects and not dipoles, the latter of which were used by several researchers in previous studies to model the noise radiated from heated coaxial jets [1]. A critical Reynolds number of 400,000 was given in [6] to avoid these effects, which agrees with the Reynolds number of the second coaxial jet in the present study. Among other objectives it is intended in this study to elucidate the temperature effects on the noise generation and on the spectral shape in the far field by a detailed analysis of the heat release and the entropy source terms in the APE formulation. The overall structure of the discussion of the noise generation mechanisms is based on three steps. Firstly, the noise computation of the single jet is presented to validate the numerical method and to discuss the influence by the different source terms, secondly, the flow field and the acoustic field of the low Reynolds number single and coaxial jet are analyzed, and thirdly, the two hot coaxial jets are investigated to determine the impact of the Reynolds number and of the different source terms of the APE-4 system on the acoustic field. This paper is organized as follows. The governing equations and the numerical procedure of the LES/APE method are described in section 2. The simulation parameters of the cold single jet and the two heated coaxial jets are given in section 3. The results for the flow field and the acoustical field are discussed in detail in section 4. Finally in section 5, the findings of the present study are summarized.

2 Governing equations and numerical methods

2.1 Large-Eddy Simulation

The large-eddy simulations of all three jets were performed by Renze and Ganeboina[7]. The discretization is based on a second-order accurate AUSM formulation for the inviscid fluxes and centered differences for the non-Euler terms. An explicit 5-step Runge-Kutta time stepping scheme is used for the temporal integration. More details can be found in Meinke et al. [8]. On the lateral boundaries, a traction-free boundary condition [9] is implemented to allow a correct jet entrainment. The outflow boundary condition uses characteristic boundary conditions and, in addition, a damping zone by a grid stretching to suppress reflections. The inflow conditions are discussed below when the parameters of the various jets are introduced.

2.2 Acoustic Perturbation Equations

The set of acoustic perturbation equations (APE) used in the present simulations corresponds to the APE-4 formulation proposed in [3]. It is derived by rewriting the complete Navier-Stokes equations as

$$\frac{\partial p'}{\partial t} + \bar{c}^2 \boldsymbol{\nabla} \cdot \left(\bar{\rho} \boldsymbol{u}' + \bar{\boldsymbol{u}} \frac{p'}{\bar{c}^2} \right) = \bar{c}^2 q_c \tag{1}$$

$$\frac{\partial \boldsymbol{u}'}{\partial t} + \boldsymbol{\nabla} \left(\bar{\boldsymbol{u}} \cdot \boldsymbol{u}' \right) + \boldsymbol{\nabla} \left(\frac{p'}{\bar{\rho}} \right) = \boldsymbol{q}_m. \tag{2}$$

The right-hand side terms constitute the acoustic sources

$$q_c = -\boldsymbol{\nabla} \cdot (\rho' \boldsymbol{u}')' + \frac{\bar{\rho}}{c_p} \frac{\bar{D} s'}{Dt} \tag{3}$$

$$\boldsymbol{q}_m = -\left(\boldsymbol{\omega} \times \boldsymbol{u} \right)' + T' \boldsymbol{\nabla} \bar{s} - s' \boldsymbol{\nabla} \bar{T} - \left(\boldsymbol{\nabla} \frac{(u')^2}{2} \right)' + \left(\frac{\boldsymbol{\nabla} \cdot \underline{\tau}}{\rho} \right)'. \tag{4}$$

To obtain the APE system with the perturbation pressure as independent variable the second law of thermodynamics in the first-order formulation is used. The left-hand side constitutes a linear system describing linear wave propagation in mean flows with convection and refraction effects. The viscous effects are neglected in the jet noise simulations. That is, the last source term in the momentum equation is dropped.

The numerical algorithm to solve the APE-4 system is based on a 7-point finite-difference scheme using the well-known dispersion-relation preserving scheme (DRP) [10] for the spatial discretization including the metric terms on curvilinear grids. This scheme accurately resolves waves longer than 5.4 points per wave length (PPW). For the time integration an alternating 5-6 stage low-dispersion low-dissipation Runge-Kutta scheme [11] is implemented.

To eliminate spurious oscillations the solution is filtered using a 6th-order explicit commutative filter [12, 13] at every tenth iteration step. As the APE system does not describe convection of entropy and vorticity perturbations [3] the asymptotic radiation boundary condition by Tam and Webb [10] is sufficient to minimize reflections on the outer boundaries. On the inner boundaries between the different matching blocks covering the LES and the acoustic domain, where the transition of the inhomogeneous to the homogeneous acoustic equations takes place, a damping zone is formulated to suppress artificial noise generated by a discontinuity in the vorticity distribution [14].

3 Simulation Parameters

The quantities u_j and c_j are the jet nozzle exit velocity and sound speed, respectively, and T_j and T_∞ the temperature at the nozzle exit and in the ambient fluid. Unlike the single jet, the simulation parameters of the coaxial jets have additional indices "p" and "s" indicating the primary and secondary stream.

At constant stagnation temperature T_0 and a temperature ratio $T_j/T_\infty = 0.86$ the Mach number of the round single jet is $M_j = U_j/c_j = 0.9$ and the Reynolds number based on the diameter of the nozzle exit is $Re = 3,600$. These parameters match with previous investigations performed by a DNS by Freund [4] and experiments by Stromberg et al. [5].
The coaxial jets have a velocity ratio of the secondary and primary jet exit velocity of $\lambda = U_s/U_p = 0.9$, a Mach number 0.9 and 0.62 for the secondary and the primary stream, respectively, a temperature ratio of $T_s/T_p = 0.37$ and a jet exit radius ratio of $r_s/r_p = 2.0$. The static temperature of the secondary stream is equal to the ambient temperature.

The inflow conditions of all three jets are described by a hyperbolic-tangent profile for the velocity and the density profile reading

$$u(r) = \frac{U_j}{2} + \frac{U_j}{2}\tanh(\frac{r_0 - r}{2\theta_m}) \tag{5}$$

$$\tag{6}$$

for the single jet with nozzle radius r_0 and a initial momentum thickness of the shear layer $\frac{\theta_m}{r_0} = 0.05$ in eqn.(5) and

$$u(r) = \frac{U_p + U_s}{2} + \frac{U_p - U_s}{2}\tanh(\frac{r_p - r}{2\theta_m}), \quad (\text{if} \quad r \leq 1.08 r_p) \tag{7}$$

$$u(r) = \frac{U_s}{2} + \frac{U_s}{2}\tanh(\frac{r_s - r}{2\theta_m})), \quad (\text{if} \quad r > 1.08 r_p) \tag{8}$$

$$\rho(r) = \frac{\rho_p + \rho_s}{2} + \frac{\rho_p - \rho_s}{2}\tanh(\frac{r_p - r}{2\theta_m}) \tag{9}$$

for the coaxial jets. The ratio between the initial momentum thickness of the shear layer and the primary jet radius is specified according to the velocity and gradients existing in the primary and secondary shear layers. A ratio of $\frac{\theta_m}{r_p} = 0.025$ is used in eqn.(7) and 0.05 in the eqs.(8) and (9).

Small random perturbations similar to those in the single jet simulation are inserted into both shear layers over a short distance at $x/r_p = 0.8$ from the inflow boundary. The lateral and outflow boundary conditions remain unchanged with respect to the single jet calculation.

For the single jet instantaneous data are sampled over a period of $\bar{T}_s = 1265 \cdot \Delta t_s \cdot c_\infty/r_0 = 128.83$, where $\Delta t_s \cdot c_\infty/r_o$ is the sampling rate and c_∞ is the ambient sound speed at the exit of the nozzle. This period corresponds to approximately 2.5 times the time interval an acoustic wave needs to propagate through the computational domain.The sampling rate suffices to resolve a maximum Strouhal number of 1.81 using a minimum of $\frac{T_{min}}{\Delta t} = 12$ points per period.

For the coaxial jets instantaneous data are sampled over a period of $\bar{T}_s = 2000 \cdot \Delta t \cdot c_\infty / r_s = 83$. This period corresponds roughly 2.6 times the time interval an acoustic wave needs to propagate through the computational domain. As in the single jet computation, the source terms are cyclically inserted into the acoustic simulation.

The main grid parameters for the single jet and the two coaxial jet simulations of the flow field and the acoustical field defining the minimum and maximum grid spacing in the streamwise and spanwise direction are given Tab. 1. For the acoustic grid of the coaxial jets the same grid topology and grid spacing was used. However, the domain size was slightly extended in the radial direction.

	LES (Source Domain)	APE
Single Jet, Re 3,600	$\frac{\Delta x_{min}}{r_0} = 0.13$	const. $\frac{\Delta x}{r_0} = 0.2$
Single Jet, Re 3,600	$\frac{\Delta x_{max}}{r_0} = 0.18$	
Single Jet, Re 3,600	$\frac{\Delta r_{min}}{r_0} = 0.045$	$\{\Delta y, \Delta z\}_{min} = 0.095$
Single Jet, Re 3,600	$\frac{\Delta r_{max}}{r_0} = 0.26$	$\{\Delta y, \Delta z\}_{max} = 0.3$
Coaxial Jet, Re 3,600	$\frac{\Delta x_{min}}{r_s} = 0.07$	$\frac{\Delta x_{min}}{r_s} = 0.125$
Coaxial Jet, Re 3,600	$\frac{\Delta x_{max}}{r_s} = 0.09$	$\frac{\Delta x_{max}}{r_s} = 0.25$
Coaxial Jet, Re 3,600	$\frac{\Delta r_{min}}{r_s} = 0.04$	$\{\Delta y, \Delta z\}_{min} / r_s = 0.05$
Coaxial Jet, Re 3,600	$\frac{\Delta r_{max}}{r_s} = 0.16$	$\{\Delta y, \Delta z\}_{max} / r_s = 0.15$
Coaxial Jet, Re 400,000	$\frac{\Delta x_{min}}{r_s} = 0.07$	$\frac{\Delta x_{min}}{r_s} = 0.125$
Coaxial Jet, Re 400,000	$\frac{\Delta x_{max}}{r_s} = 0.07$	$\frac{\Delta x_{max}}{r_s} = 0.25$
Coaxial Jet, Re 400,000	$\frac{\Delta r_{min}}{r_s} = 0.02$	$\{\Delta y, \Delta z\}_{min} / r_s = 0.05$
Coaxial Jet, Re 400,000	$\frac{\Delta r_{max}}{r_s} = 0.10$	$\{\Delta y, \Delta z\}_{max} / r_s = 0.15$

Table 1: LES and CAA grid specifications for the Mach 0.9 and Reynolds number 3,600 cold single jet and for the Mach 0.9 and Reynolds number 3,600 and 400,000 heated coaxial jets.

4 Results

The results of the present study are divided into two parts. First, the flow field of the cold low Reynolds number single jet and the heated low and high Reynolds number coaxial jets will be discussed concerning the mean flow properties and the turbulent statistics. To relate the findings of the coaxial jet to the single jet, the flow field of which has been sucessfully validated in previous studies [7] against the experimental results by Stromberg et al. [5] and numerical results by Freund [4], comparisons to the flow field properties of the single jet computation are drawn. The second part comprises a discussion on the results of the acoustic field. Firstly, the impact of different source terms of the low

Reynolds number single jet on the sound field will be discussed. Note, the acoustical data are compared with findings from [20] at Reynolds numbers 2,500 and 5,000 since no other acoustical results are available in the near field of the Ma 0.9 jet. Secondly, the acoustic field of the low Reynolds number single and coaxial jets will be compared. Finally, the acoustic field of the two coaxial jets will be investigated in more detail concerning the influence of the Reynolds number and the impact by the additional source terms of the APE system, which are related to heating effects.

4.1 Flow Field

The initial region of the coaxial jet consists of two potential cores, a primary mixing region between the primary and the secondary jet, and a secondary mixing region between the secondary jet and the ambient air. Similar to the single jet, the coaxial jet can be divided into three zones. The initial merging zone defines the region from the nozzle exit up to the location of the end of the secondary potential core. The zone, which is characterized by the mixing of the primary and the secondary stream, is called intermediate zone. This zone is followed by the fully merged or self similar zone.

To analyze the flow field and the acoustical field in the subsequent section, we computed at various planes normal to the jet axis the profiles of the mean flow, the Reynolds stresses, and the fluctuating source terms of the APE system. These profiles were uniformly distributed in the axial direction from $x/r_s = 0$ to $x/r_s = 18$ as shown in Fig. 1 by the dashed lines. The solid lines are the streamlines indicating a proper entrainment from the lateral boundaries. However, test cases have shown when the lateral boundaries are placed too close to the jet axis, the flow field computation becomes unstable. If the placement of the radial boundaries are sufficiently large from the jet axis the simulation runs stable.

First, the development of the mean flow of the single jet and the coaxial jets is shown in Figs. 2(a) and (b) by the density and axial velocity distributions based on the nozzle exit values of the secondary jet. Both coaxial jets show almost an identical mean flow development independently from the chosen Reynolds numbers. The main reason for this resemblence is that in both jet simulations the same initial shear layer momentum thickness was used. The chosen initial momentum thickness is based on that used by Bogey and Bailly [15] for a cold single jet at the same Reynolds number. In doing so it is possible to compare single and coaxial jets at the same Reynolds number and to stress the impact of temperature gradients on the acoustic sources.

In the initial coaxial jet exit region the mixing of the primary shear layer takes place. Because of the small velocity ratio of the primary and the secondary jet this mixing region extends only up to $x = 6r_s$. During the mixing process, the edges of the initially sharp density profiles get smoothed. Further downstream the secondary jet shear layers start to break up causing a rapid exchange and mixing of the fluid in the inner core. This can be seen by the fast decay of the mean density profiles in Fig. 2(a). The breakup process enhances probably the mixing process yielding higher levels of turbulent kinetic energy. It will be shown in the subsequent section that the noise levels of the present coaxial jets exceed drastically the noise levels from the single jet.

Unlike the density profiles, the mean axial velocity profile decreases only slowly. The comparison of the center line velocity decay of the single and the coaxial jet is shown in Fig. 3. It can be observed that the jet potential core length shortens with the heating of the primary jet resulting in a decreased Mach number. In the self-similar region the center line velocity decay of the single and the coaxial jet is similar. According to Champagne and Wygnanski [17], the following reference scales U_{ref}, r_{ref}, and ρ_{ref} representing the reference velocity, radius, and density are defined to compare the coaxial jet simulation results with the single jet simulation results

$$U_{ref} = \sqrt{\frac{\rho_s A_s U_s^2 + \rho_p A_p U_p^2}{\rho_s A_s + \rho_p A_p}} \tag{10}$$

$$r_{ref} = \frac{\sqrt{\frac{\rho_s A_s U_s^2 + \rho_p A_p U_p^2}{\rho_s U_s^2 + \rho_p U_p^2}}}{\pi} \tag{11}$$

$$\rho_{ref} = \frac{\rho_s A_s U_s^2 + \rho_p A_p U_p^2}{A_s U_s^2 + A_p U_p^2}. \tag{12}$$

The coaxial jet data were axially shifted to have the common potential core collapse $\frac{x_c}{r_{ref}}$. The inverse of the center line velocity of the single and coaxial jets is shown in Fig. 4(a). The axial coordinate is taken as $\frac{x-x_s}{2r_{ref}}$, with the virtual origin $x_s = x_0$ for the single jet and $x_s = x_0 +$ axial shifting for the coaxial jet. The data fairly collapse on each other, which indicates similarity. In Fig. 4(b) the half-velocity radius, non-dimensionalized by the length scale $r_{ref}\sqrt{\frac{\rho_\infty}{\rho_{ref}}}$, is displayed for single and coaxial jets showing again a good agreement, which exhibits self-similarity and an accurate jet evolution. The differences in the initial regions close to the nozzle are caused by the discrepancy in the reference radius and the original nozzle radius.

Both coaxial jets show a similar development of the Reynolds stresses $\sigma_{uu} = \frac{1}{T}\int (u'u')\,dt$ and $\sigma_{uv} = \frac{1}{T}\int (u'v') dt$ with u' and v' based on the secondary axial exit velocity u_s at different axial cross sections in Figs. 5 (a) and (b) ranging from $x/r_s = 3$ to $x/r_s = 21$. The mixing process is clearly enhanced in the coaxial jet compared to the single jet case. The axial velocity fluctuations of the coaxial jets start to increase at $x/r_s = 3$ and reach at $x/r_s = 6$ high levels on the center line and in the outer shear layers, while the single jet axial fluctuations start to develop not before $x/r_s = 9$. This difference is caused by the density and entropy gradient, which is the driving force of this process. This is confirmed by the velocity decay on the jet center line in Fig. 3, which starts near $x/r_s = 3$ for the heated coaxial jet and at $x/r_s = 7$ for the cold single jet, and also in Fig. 2(a) by the mean density profiles. These profiles are redistributed beginning at $x/r_s = 3$ until they take on a uniform shape at approx. $x/r_s = 9$. When this process is almost finished the mixing of the mean axial velocity profile sets in between $x/r_s = 6$ and $x/r_s = 9$.

This redistribution evolves much slower over several radii in the downstream direction. Furthermore, note that the inflow forcing in the coaxial jet simulation was applied to both shear layers between the primary and secondary stream and between the secondary stream and the ambient flow, while in the single jet simulation only one shear layer was excited by the inflow forcing.

4.2 Acoustics

The presentation of the acoustical results is organized as follows. First, the main characteristics of the acoustic field of the single jet from previous noise [18],[19] computations are summarized, by which the present hybrid method has been successfully validated against. Then, the acoustic fields for the single and coaxial jets are briefly discussed at two observer points. Finally, a detailed investigation follows comprising the impact of different source terms and the Reynolds number dependence on the acoustical solution of the heated coaxial jets.

Unlike the direct acoustic approach by an LES or a DNS, the hybrid methods based on an acoustic analogy allows to separate different contributions to the noise field. These noise mechanisms are encoded in the source terms of the acoustic analogy and can be simulated separately exploiting the linearity of the wave operator. Previous investigations of the single jet noise demonstrated the fluctuating Lamb vector to be the main source term for cold jet noise problems. An acoustic simulation with the Lamb vector only was performed and the sound field at the same points were computed and compared with the solution containing the complete source term. The overall acoustic field is shown in Fig. 6 by instantaneous pressure contours in the near field, i.e., outside the source region, and contours of the Lamb vector in the acoustic source region. The acoustic field is dominated by long pressure waves radiating in the downstream direction. The arrows indicate the assumed location of the noise generation by tracing back the radiation directions of the strongest pressure waves. The impact of the various source formulations, i.e., complete source vs. Lamb vector only, on the overall sound pressure level OASPL in Fig. 7(a) is mainly evident for the noise between $x/R = 22.0$ and $x/R = 28.0$. However, even in this region the OASPL differs by only up to 1dB. The acoustic pressure distribution in Fig. 7(b) at the downstream observer point is almost identical corroborating the Lamb vector to be the dominant source for cold jet noise.

In the following, the change of the acoustic field for the low Reynolds number cold single and heated coaxial jet is discussed. The acoustic field was computed at two observer locations on the same line as in Fig. 7 at a distance of 15 radii from the jet axis based on the outer jet radius. In Tab. 2 the overall sound pressure level and the peak frequency of the pressure spectrum are given. The OASPL differs by more than 15 dB for the first observer location and 12 dB for the second observer location. The change in the mean flow development and in the turbulence statistics between the single and the coaxial jet is clearly evidenced in the noise levels. It is believed that the enhanced entrainment process in the initial region of the coaxial jet forced by the density and temperature gradient is a main contributor to the increased sound in the near field.

	OASPL $\frac{x}{r_s}=11,\ \frac{r}{r_s}=15$	f_{peak} $\frac{x}{r_s}=11,\ \frac{r}{r_s}=15$	OASPL $\frac{x}{r_s}=30,\ \frac{r}{r_s}=15$	f_{peak} $\frac{x}{r_s}=30,\ \frac{r}{r_s}=15$
Single Jet	119.5 dB	$St = 0.18$	126.5 dB	$St = 0.18$
Coaxial Jet	135 dB	$St = 0.26$	138.5	$St = 0.26$

Table 2: Comparison of the acoustic field of the cold single and heated coaxial jet at Re= 3,600.

Subsequently, the acoustic field of the heated coaxial jets will be analyzed. Unlike in the cold jet simulation, in the heated coaxial jets additional source terms besides the Lamb vector $L' = -\left(\epsilon_{ijk}\omega_j u_k\right)'$ become important. These are the heat release term $\frac{\bar{c}^2\bar{\rho}}{c_p}\frac{\bar{D}s'}{Dt}$ and the temperature and entropy fluctuation expression $T'\frac{\partial\bar{s}}{\partial x_i} - s'\frac{\partial\bar{T}}{\partial x_i}$. The acoustic field by the Lamb vector only is shown in Fig. 8(a) for the low Reynolds number jet and in Fig. 8(b) for the high Reynolds number jet. Both jets predominantly radiate acoustic waves in the downstream direction. The high Reynolds number jet, however, shows some high frequency waves radiating in the direction normal to the jet axis as it is characteristic for high Reynolds number jets. Figs. 8(c) and (d) display the acoustic field generated by the heat release and entropy and temperature fluctuations for the low and the high Reynolds number jet. The pressure contours show a strong Reynolds number dependence. Unlike the low Reynolds number jet, the high Reynolds number jet radiates strongly at obtuse angles, i.e., in the direction perpendicular to the jet axis, while the downstream region is almost silent. Especially in the high Reynolds number case the heating effect by the temperature gradient emphasizes a dipole-like noise generation.

In the following Figs. 9 and 10 are discussed, first with emphasis on the Lamb vector findings, then by considering the impact of the heat release and the temperature and entropy fluctuations. The predicted near field is shown by the overall sound pressure levels in Fig. 9 along an arc of radius $R = 25r_s$ from the jet nozzle. The angle θ was measured from 15^o to 90^o in three-degree increments from the streamwise direction. The sound pressure values are averaged on 30 equally distributed points in the azimuthal direction at a given observer location on the directivity arc. The contribution by the Lamb vector only in Fig. 9(a) and (b) for the low and the high Reynolds number jets shows that both coaxial jets radiate at approximately the same strength in the 30^o direction from the jet center line. In both cases the OASPL by the Lamb vector is very close to that of the complete source.

The pressure field in the downstream direction, i.e., at 30^o, is mainly generated by low-frequency waves at Strouhal number $St = f \cdot D_s/u_s \approx 0.25$ based on the outer jet diameter and the secondary axial jet exit velocity as can be seen from Fig. 10(a). For larger radiation angles the pressure spectrum, defined by the Fourier transformed of the complex and conjugate complex pressure signal $SPL = \hat{p}\hat{p}^*$, broadens particularly for the high Reynolds number jet. The peak location of the maximum pressure value at a 55^o

radiation angle of the low Reynolds number jet is at $St \approx 0.37$, whereas the high Reynolds number jet shows distinct peak values up to $St \approx 0.6$. This observation is in agreement with the common assumption that low frequency waves are generated independently from the Reynolds number in the downstream direction, while high frequency waves depend on the Reynolds number. That is, the increase of the Reynolds number substantially generates smaller structures in the shear layers, which contribute to a broadbanded noise in the plane normal to the jet axis. This observation coincides with findings from Bogey and Bailly [20].

The acoustic field by the source terms related to the density and temperature gradient, referred to in the following as entropy sources, are also displayed in Figs. 9(a) and (b) for the low and the high Reynolds number coaxial jet. The shape of the OASPL is characterized by the dipole-like behavior of the source. The deviation from a perfect dipole shape is determined by the location of the center of the directivity circle, which is located at $x \approx 11r_s$, i.e., eleven radii upstream from the assumed center of the noise generation by the entropy terms in Fig. 8(d). The additional noise radiation from the high Reynolds number jet grows at increasing angle θ compared to the low Reynolds number jet. Only in the direction normal to the jet axis and only for the high Reynolds number jet the overall sound pressure level approaches the noise level from the acoustic field computed by the Lamb vector. From Fig. 9 it can be concluded that the overall sound pressure level is dominated by the Lamb vector. This is definitely valid in the low Reynolds number case and for the high Reynolds number jet when the range $20^o \leq \theta \leq 60^o$ is considered. The pressure spectra by the entropy sources in Fig. 10(b) exhibit a more broadbanded spectrum without a distinct peak for different radiation angles. In general, the maximum pressure values are reached at Strouhal numbers greater than 0.3, which is above that of the Lamb vector.

To define the streamwise location of the main noise generation, profiles of the fluctuation levels of the different source terms are shown in Fig. 11 in equidistant planes perpendicular to the jet axis ranging from $x/r_s = 3$ to $x/r_s = 18$ for the root mean square (rms) of the magnitude of the Lamb vector $L' = -\left(\epsilon_{ijk}\omega_j u_k\right)'$, the temperature and entropy fluctuations $T'\frac{\partial \bar{s}}{\partial x_i} - s'\frac{\partial \bar{T}}{\partial x_i}$, and the heat release $\frac{\bar{c}^2\bar{\rho}}{c_p}\frac{\bar{D}s'}{Dt}$ terms. The fluctuation levels generated by the Lamb vector in Fig. 11(a) grow quite extensively in the initial merging zone in the two shear layers of the coaxial jets, while the cold single jet remains quiet in this region. The primary and the secondary shear layers of the coaxial jets merge such that only one extremum remains, which is located in the outer shear layer. Further downstream, the profiles broaden and the peak location moves to the center line axis. The fluctuation levels of the Lamb vector of the high Reynolds number jet clearly exceed those of the low Reynolds number jet. This is remarkable since the noise levels produced by the Lamb vector in Fig. 9 are similar for both jets. This indicates that the dynamics of the Lamb vector and not only its absolute fluctuation value is important. This is also confirmed by the observation that the fluctuation levels of the single jet are roughly of the order of those of the coaxial jet at the same Reynolds number, whereas the sound levels differ by up to 15 dB.

The fluctuation levels generated by the temperature and entropy fluctuations in Fig. 11(b) and the heat release in Fig. 11(c) show a strong Reynolds number dependence. Unlike the heated coaxial jets the cold single jet is quiet for these source terms. The Reynolds number effect becomes evident in both source terms, which are relatively quiet for the Reynolds number 3,600 jet, while the high Reynolds number jet shows distinct structures. The heat release profile grows in the inner shear layer where the mixing process due to the temperature and the density gradient is generated. Further downstream a second peak on the center line is formed at $x/r_s = 6$, at which also the temperature and entropy fluctuations in the inner shear layer Fig. 11(b) become dominant. In this region cold ambient fluid is entrained as it can be seen in the mean density profile in Fig. 2(a) exciting the source terms related to the heating effect. The temperature and entropy fluctuations do occur only within a small region between $x/r_s = 3$ and $x/r_s = 9$ and in the inner shear layer, while the heat release source term possesses a pronounced distribution between $x/r_s = 3$ and $x/r_s = 15$ and broadens quite excessively in the radial direction.

5 Conclusions

In the present paper we computed three different jets, a cold single jet at $Ma = 0.9$ and Reynolds number $3,600$ and two coaxial jets at $Ma_s = 0.9$ and at Reynolds number $3,600$ and $400,000$ based on the outer diameter. The computed flow fields and acoustical fields differed significantly between the single and the two coaxial jets. The coaxial jets showed an enhanced exchange and mixing of the fluid in the initial region of the jet due to the density and temperature gradient. Compared to the single jet higher turbulent fluctuation levels were produced in the shear layers and on the center line generating high noise levels in the near field. The dominant source term in the APE formulation for the cold single jet has been shown to be the Lamb vector, while for the coaxial jets additional source terms of the APE-4 system due to heating effects must be taken into account. These source terms are generated by temperature and entropy fluctuations and by heat release effects and radiate dipole-like to the far field. This dipole-like structure mainly occurs in the plane perpendicular to the jet axis and is Reynolds number dependent. The radiation to the far field is more effective for the higher Reynolds number coaxial jet. The analysis of the fluctuation energy of the source terms shows distinct differences in the development of the Lamb vector between the cold single and the heated coxial jet. Since the Lamb vector is the major contributor to the acoustic field, the generated sound pressure levels differ strongly. However, the present investigation shows that the noise levels in the far field are not directly connected to the fluctuation levels of the source terms. To study the dynamics of the source terms the proper orthogonal decomposition (POD) method will be applied to the source terms in future studies. First results on the singe jet can be found in [21] and will be extended to the coaxial jets.

6 Acknowledgments

The present work was funded by the Deutsche Forschungsgemeinschaft and the Centre National de la Recherche Scientifique (DFG-CNRS) in the framework of the subproject "Noise Prediction for a Turbulent Jet" of the research group 508 "Noise Generation in Turbulent flows". The APE solutions were computed with the DLR PIANO code the development of which is part of the cooperation between DLR Braunschweig and the Institute of Aerodynamics of RWTH Aachen University.

REFERENCES

[1] Fisher, M.J. Preston, A., "A modelling of the noise from simple coaxial jets, part II: With heated primary flow." *J. Sound Vibration*, Vol. 209, No. 3, 1998, pp. 405–417.

[2] Andersson, N., Eriksson, L.-E., and Davidson, L., "LES Prediction of Flow and Acoustcial Field of a Coaxial Jet." Paper 2005-2884, AIAA, 2005.

[3] Ewert, R. and Schröder, W., "Acoustic pertubation equations based on flow decomposition via source filtering," *J. Comput. Physics*, Vol. 188, 2003, pp. 365–398.

[4] Freund, J., "Noise sources in a low-Reynolds-number turbulent jet at Mach 0.9," *J. Fluid Mech.*, Vol. 438, 2001, pp. 277–305.

[5] Stromberg, J., McLaughlin, D., and Troutt, T., "Flow field and acoustic properties of a Mach number 0.9 jet at a low Reynolds number," *J. Sound Vibration*, Vol. 72, 1980, pp. 159–176.

[6] Viswanathan, K., "Aeroacoustics of hot jets," *J. Fluid Mech.*, Vol. 516, 2004, pp. 39–82.

[7] Ganeboina, S. and Renze, P., "Large eddy simulation of subsonic turbulent jets," Internal Report IB-AIA-2005-5, Institute of Aerodynamics, RWTH Aachen, 2005.

[8] Meinke, B. J., Schröder, W., Krause, E., and Rister, T., "A Comparison of Second- and Sixth-Order Methods for Large-Eddy Simulations," *submitted to Comput. & Fluids*, Vol. 21, 2002, pp. 695–718.

[9] Boersma, B. J., Brethouwer, G., and Nieuwstadt, F. T. M., "A numerical investigation on the effect of the inflow conditions on a self-similar region of a round jet," *Phys. Fluids*, Vol. 10, No. 4, 1998, pp. 899–909.

[10] Tam, C. K. W. and Webb, J. C., "Dispersion-Relation-Preserving Finite Difference Schemes for Computational Acoustics," *J. Comput. Physics*, Vol. 107, No. 2, 1993, pp. 262–281.

[11] Hu, F. Q., Hussaini, M. Y., and Manthey, J. L., "Low-Dissipation and Low-Dispersion Runge-Kutta Schemes for Computational Acoustics," *J. Comput. Physics*, Vol. 124, No. 1, 1996, pp. 177–191.

[12] Shang, J. S., "High-order compact-difference schemes for time dependent maxwell equations," *J. Comput. Physics*, Vol. 153, 1999, pp. 312–333.

[13] Vasilyev, O. V., Lund, T. S., and Moin, P., "A general class of commutative filters for LES in complex geometries," *J. Comput. Physics*, Vol. 146, 1998, pp. 82–104.

[14] Schröder, W. Ewert, R., "On Concepts of LES-CAA Coupling," *Large-Eddy Simulations for Acoustics*, edited by Hüttl, Wagner, and Delfs, Cambridge University Press, 2005.

[15] Bogey, C. and Bailly, C., "Effects of Inflow Conditions and Forcing on Subsonic Jet Flows and Noise," *AIAA Journal*, Vol. 43, 2005, pp. 1000–1007.

[16] Lockard, D., "An efficient, two-diemnsional implementation of the Ffowcs Williams and Hawkings equation," *J. Sound Vibration*, Vol. 229, No. 4, 2000, pp. 897–911.

[17] Champagne, F. and Wygnanski, I., "An experimental investigation of coaxial turbulent jets," *Int. J. Heat & Mass Transfer*, Vol. 14, 1971, pp. 1445–1464.

[18] Gröschel, E., Meinke, M., and Schröder, W., "Noise Prediction for a Turbulent Jet Using an LES/CAA Method." Paper 2005-3039, AIAA, 2005.

[19] Gröschel, E., Schröder, W., Renze, P., Meinke, M., and Comte, P., "Noise Prediction for a Turbulent Jet Using Different Hybrid Methods," *submitted to Comput. & Fluids*, 2006.

[20] Bogey, C. and Bailly, C., "Investigation of subsonic jet noise using LES : Mach and Reynolds number effects," Paper 2004-3023, AIAA, 2004.

[21] Gröschel, E., Schröder, W., Noack, B., Schlegel, M., and Comte, P., "Reduced-order representation of turbulent jet noise," *submitted to CEMRACS Proceedings*, 2006.

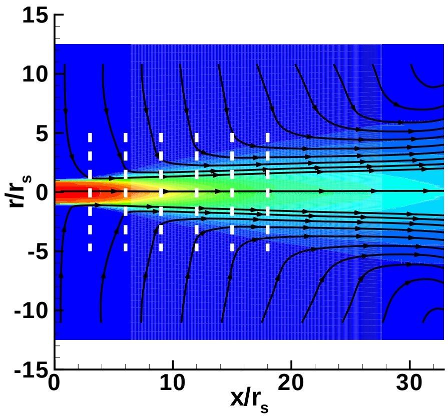

Figure 1: Visualization of the mean velocity field of the low Reynolds number jet. Stream lines indicate a proper entrainment at the lateral boundaries. White dashed lines show the location of the observer points at which the profile of various flow field and acoustical field quantities were computed.

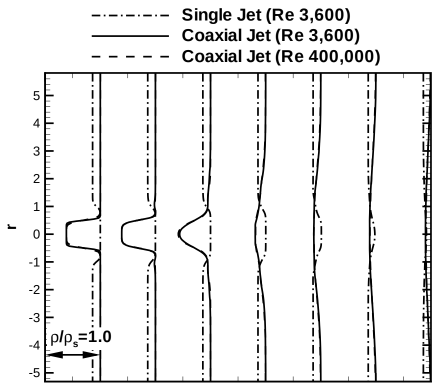

(a) Density profiles for cold single and heated coaxial jets.

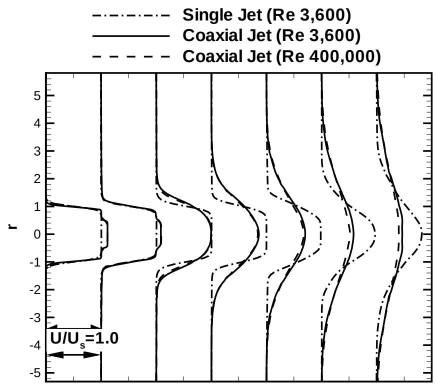

(b) Axial velocity profiles for cold single and heated coaxial jets.

Figure 2: Mean flow development in parallel planes perpendicular to the jet axis. Equally distrubuted spacing from $x/r_s = 0$ to $x/r_s = 18$.

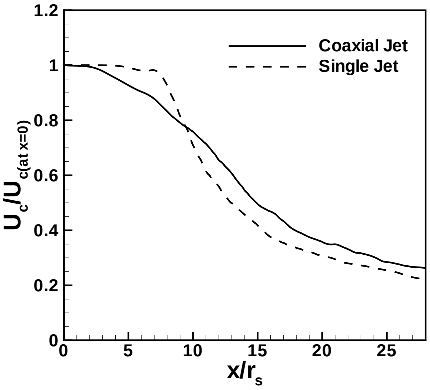

(a)

Figure 3: Center line velocity decay based on the primary jet nozzle exit velocity u_p for single and low Reynolds number coaxial jet.

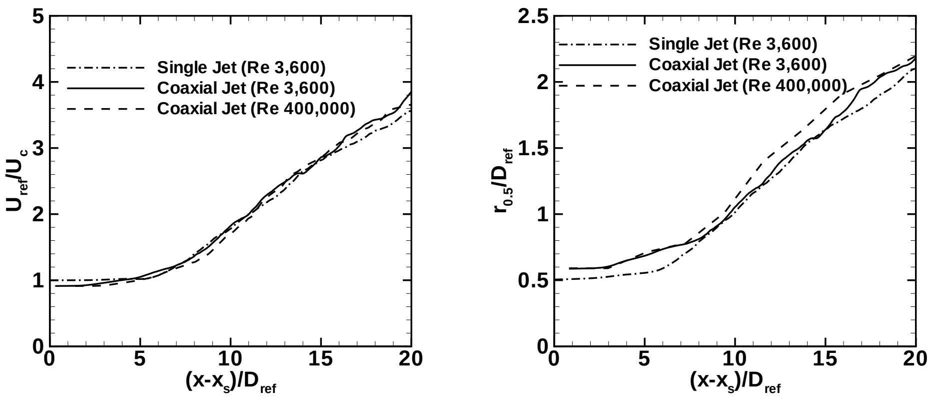

(a) The inverse of the mean center line velocity of the coaxial and the single jet (axially shifted and scaled by D_{ref}).

(b) The half-velocity radius of the coaxial and the single jet (axially shifted and scaled by D_{ref}).

Figure 4: Time averaged axial velocity profiles for cold single and heated coaxial jet.

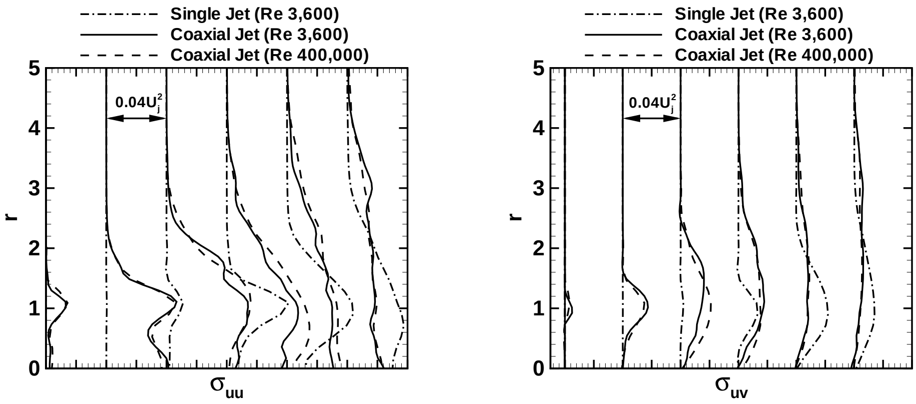

(a) Profiles of Reynold stresses σ_{uu} for cold single and heated coaxial jets.

(b) Profiles of Reynold stresses σ_{uv} for cold single and heated coaxial jets.

Figure 5: Reynolds stresses for the cold single and the heated coaxial jets.

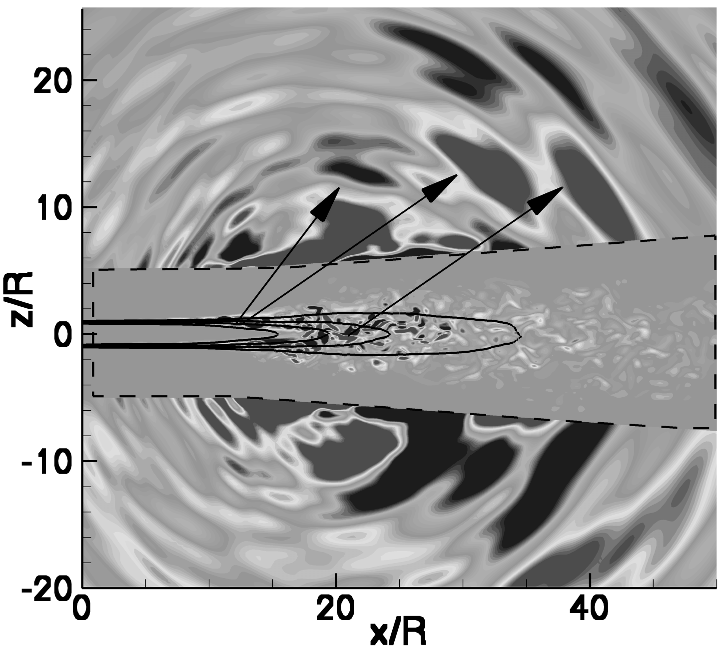

Figure 6: Pressure contours outside the source domain and the z-component of the Lamb vector inside the source domain. The solid lines show mean velocity contours for $0.95u_j$, $0.75u_j$, $0.55u_j$, and $0.35u_j$ and the arrows indicate the assumed noise generation location and the preferred radiation direction of the pressure fluctuations.

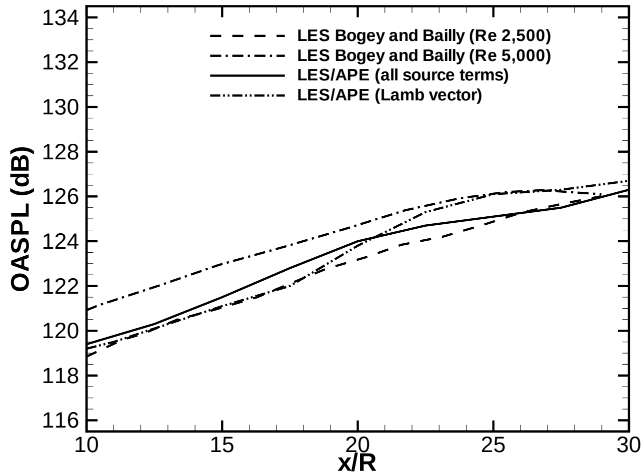

(a) Overall acoustic sound pressure level (OASPL) in dB for $r/R = 15$.

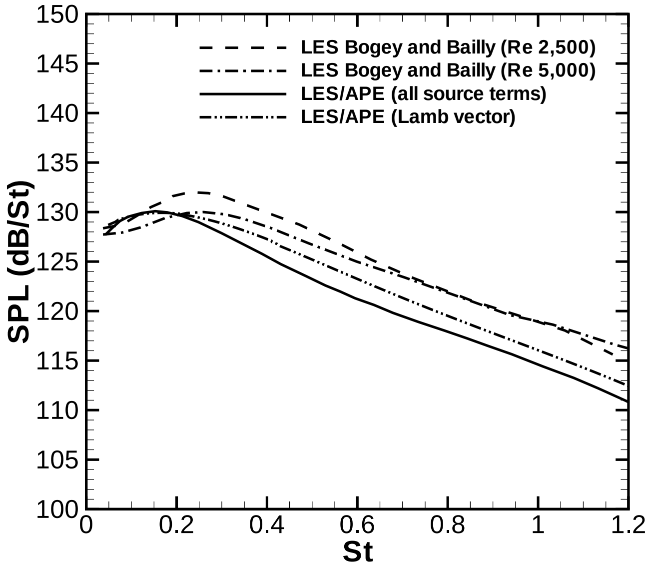

(b) LES/APE acoustic pressure spectrum in dB/St at the downstream observer point $x/R = 30$, $r/R = 15$.

Figure 7: Comparison of the acoustical field between the LES/APE solution generated by the complete source terms in eqs.(3) and (4) and by the Lamb vector $L' = -(\epsilon_{ijk}\omega_j u_k)'$. Comparison with data from Bogey and Bailly [20].

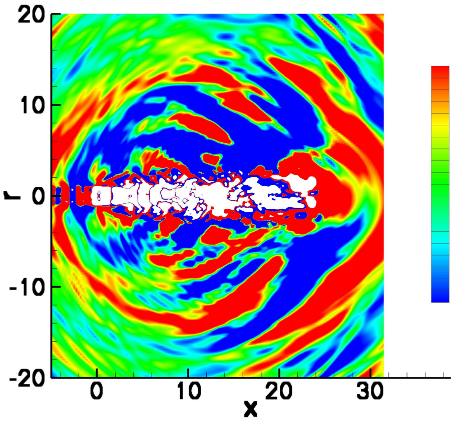

(a) Pressure contours generated by the Lamb vector $L' = -(\epsilon_{ijk}\omega_j u_k)'$ for the low Reynolds number coaxial jet.

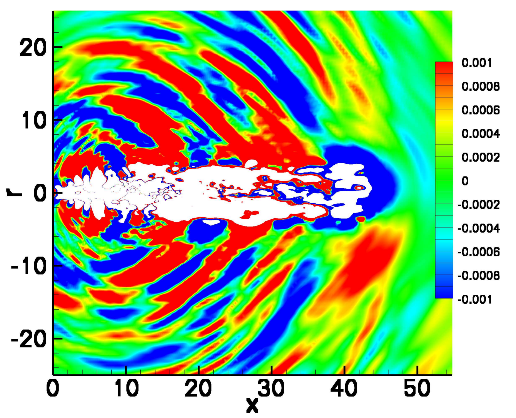

(b) Pressure contours generated by the Lamb vector $L' = -(\epsilon_{ijk}\omega_j u_k)'$ for the high Reynolds number coaxial jet.

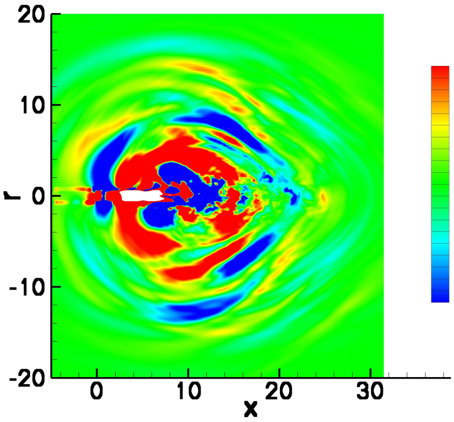

(c) Pressure contours generated by the heat release $\frac{\bar{c}^2\bar{\rho}}{c_p}\frac{\bar{D}s'}{Dt}$ and the temperature and entropy fluctuations $T'\frac{\partial \bar{s}}{\partial x_i} - s'\frac{\partial \bar{T}}{\partial x_i}$ for the low Reynolds number coaxial jet.

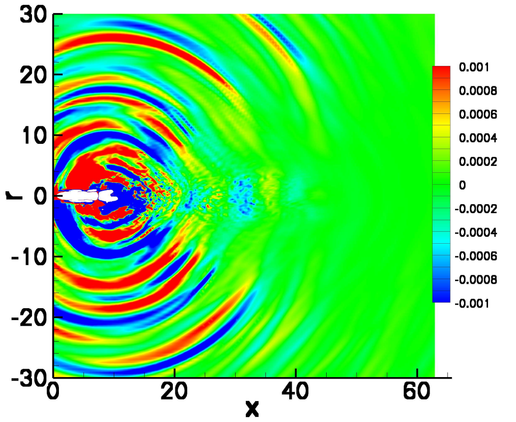

(d) Pressure contours generated by the heat release $\frac{\bar{c}^2\bar{\rho}}{c_p}\frac{\bar{D}s'}{Dt}$ and the temperature and entropy fluctuations $T'\frac{\partial \bar{s}}{\partial x_i} - s'\frac{\partial \bar{T}}{\partial x_i}$ for the high Reynolds number coaxial jet.

Figure 8: Impact of the Reynolds number and the source terms on the pressure contours of the coaxial jets.

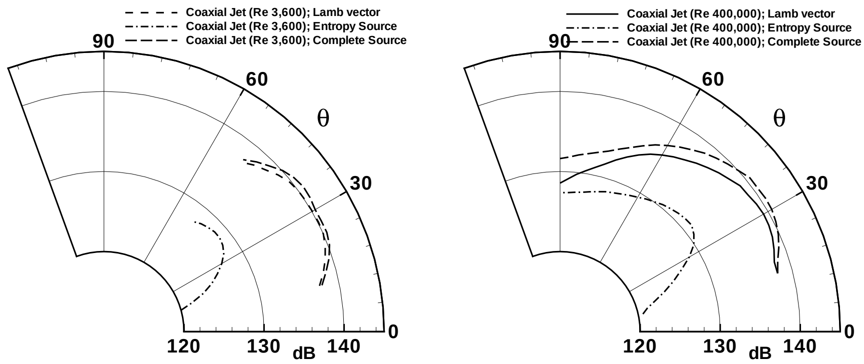

(a) Overall acoustic sound pressure level (OASPL) in dB generated by the Lamb vector $L' = -\left(\epsilon_{ijk}\omega_j u_k\right)'$, the heat release $\frac{\bar{c}^2\bar{\rho}}{c_p}\frac{\bar{D}s'}{Dt}$ and the temperature and entropy fluctuations $T'\frac{\partial\bar{s}}{\partial x_i} - s'\frac{\partial\bar{T}}{\partial x_i}$, and the complete source for the low Reynolds number jet.

(b) Overall acoustic sound pressure level (OASPL) in dB generated by the Lamb vector $L' = -\left(\epsilon_{ijk}\omega_j u_k\right)'$, the heat release $\frac{\bar{D}s'}{Dt}$ and the temperature and entropy fluctuations $T'\frac{\partial\bar{s}}{\partial x_i} - s'\frac{\partial\bar{T}}{\partial x_i}$, and the complete source for the high Reynolds number jet.

Figure 9: Predicted overall sound pressure levels for different source terms and different Reynolds numbers along an arc of radius $R = 25r_s$ from the jet nozzle.

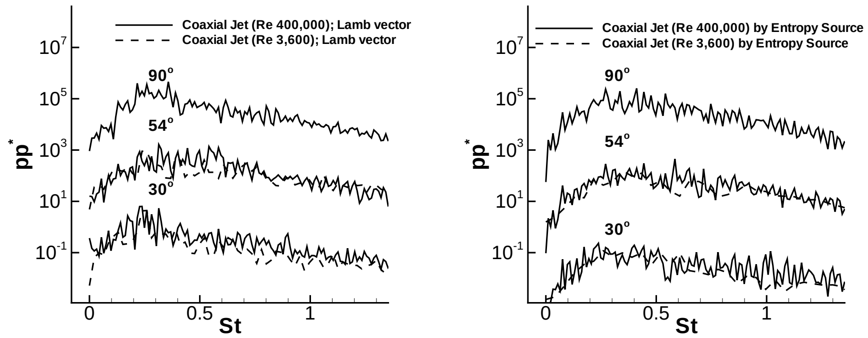

(a) Acoustic pressure spectrum, $\hat{p}\hat{p}^*$, generated by the Lamb vector $L' = -\left(\epsilon_{ijk}\omega_j u_k\right)'$ over the Strouhal number $St = f \cdot D_s/u_s$.

(b) Acoustic pressure spectrum, $\hat{p}\hat{p}^*$, generated by the heat release $\frac{\bar{c}^2\bar{\rho}}{c_p}\frac{\bar{D}s'}{Dt}$ and the temperature and entropy fluctuations $T'\frac{\partial\bar{s}}{\partial x_i} - s'\frac{\partial\bar{T}}{\partial x_i}$ over the Strouhal number $St = f \cdot D_s/u_s$.

Figure 10: The data has been staggered by multiplying the amplitude by 10^n, where $n = (\frac{\theta-30}{30})$. The angle θ was measured from 15^o to 90^o in three degree-increments from the streamwise direction and averaged on 30 equally distributed points in azimuthal direction at a given observer location on an arc of radius $R = 25r_s$ from the jet nozzle.

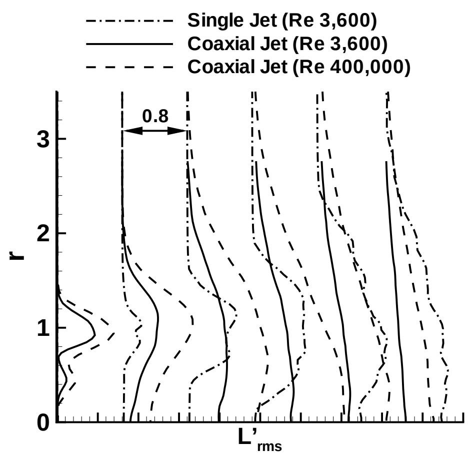

(a) RMS profiles of the Lamb vector $L' = -(\epsilon_{ijk}\omega_j u_k)'$ for cold single and two heated coaxial jets.

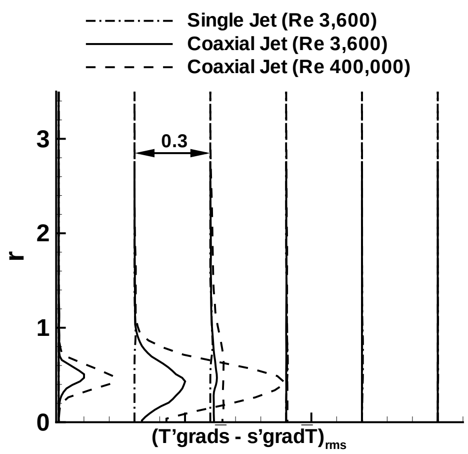

(b) RMS profiles of the temperature and entropy fluctuations $T'\frac{\partial \bar{s}}{\partial x_i} - s'\frac{\partial \bar{T}}{\partial x_i}$ for cold single and two heated coaxial jets.

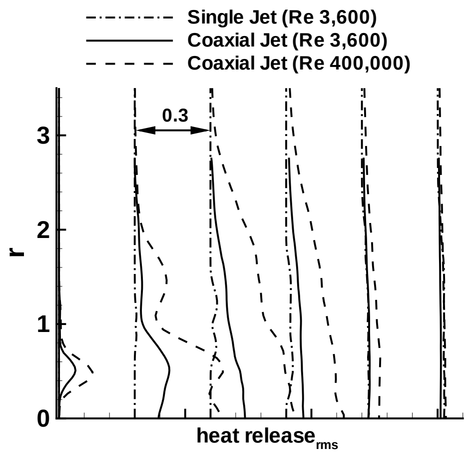

(c) RMS profiles of the heat release $\frac{\bar{c}^2\bar{\rho}}{c_p}\frac{\bar{D}s'}{Dt}$ for cold single and two heated coaxial jets.

Figure 11: Radial distributions of the various terms of the APE-4 source at different axial locations.